J Braz. Soc. Mech. Sci. Eng. (2016) 38:2129–2148
DOI 10.1007/s40430-016-0493-y

TECHNICAL PAPER

Effect of the centrifugal force on the electromechanical instability of U-shaped and double-sided sensors made of cylindrical nanowires

M. Keivani[1] · R. Gheisari[2] · A. Kanani[3] · N. Abadian[4] · J. Mokhtari[5] · R. Rach[6] · M. Abadyan[7]

Received: 8 June 2015 / Accepted: 20 January 2016 / Published online: 20 February 2016

Abstract The U-shaped and double-sided nanostructures are promising for developing miniature angular speed sensors. While the electromechanical instability of conventional beam-type nanostructures has been extensively addressed in the literature, few researchers have investigated this phenomenon in the double-sided and U-shaped sensors. In this regard, the present work demonstrates the effect of the centrifugal force on the pull-in performance of the double-sided and U-shaped sensors fabricated from cylindrical nanowire and operated in the van der Waals (vdW) regime. Based on the modified couple stress theory, the size-dependent constitutive equations of the sensors are derived. The governing equations are solved by two different approaches, i.e. the analytic Duan–Adomian method and the numerical differential quadrature method. The influences of the vdW and centrifugal forces, geometric parameters and the size phenomenon on the pull-in parameters are demonstrated.

Keywords U-shaped sensor · Double-sided sensor · Centrifugal force · Cylindrical nanowire · vdW force · Adomian decomposition method

Communicated by Eduardo Alberto Fancello.

✉ M. Abadyan
abadyan@yahoo.com

[1] Shahrekord University of Medical Sciences, Shahrekord, Iran

[2] Physics Department, Persian Gulf University, Bushehr 75169, Iran

[3] Ionizing and Non-Ionizing Radiation Protection Research Center, Paramedical Sciences School, Shiraz University of Medical Sciences, Shiraz, Iran

[4] Department of Mathematics, Isfahan (Khorasgan) Branch, Islamic Azad University, Isfahan, Iran

[5] Department of Mathematics, Isfahan (Khorasgan) Branch, Islamic Azad University, Isfahan, Iran

[6] 316 South Maple Street, Hartford, MI 49057-1225, USA

[7] Shahrekord Branch, Islamic Azad University, Shahrekord, Iran

1 Introduction

Beam-type micro/nano-electromechanical systems (MEMS/NEMS) are increasingly used in several branches of engineering and science, i.e. mechanics, chemistry, optics, biology, photonics, electronics, etc. Modeling of the electromechanical stability of NEMS is crucial for the reliable design, fabrication and operation of these devices. Many researchers have investigated the pull-in instability of NEMS devices [1–5]. Although there are many articles focused on modeling the pull-in instability of the conventional NEMS with a simple beam-type electrode [6, 7], few efforts have been made for modeling this phenomenon in less conventional systems such as the U-shaped and double-sided NEMS. In this regard, the present research is devoted to the theoretical study of the electromechanical performance of U-shaped and double-sided cantilever NEMS sensors.

The U-shaped configuration consists of two parallel cantilever micro/nano-beams with a rigid plate attached to their free ends. Recently, several studies have investigated the limitations and potential of the U-shaped MEMS/NEMS as sensors [8], actuators [9], and switches [8–11]. Qian et al. [10] developed a U-shaped nanoelectromechanical switch consisting of a capacitive plate supported by two silicon nanowires. They presented several remarkable advantages of the U-shaped switch such as decreasing the

actuation voltage, generation of higher electrostatic force, high flexibility, a high ON/OFF current ratio and a repeatable switching behavior [10]. Yan [9] and coworkers evaluated the use of the U-shaped actuator as a variable capacitor. They showed that the U-shaped nanostructure provides a larger deflection with an improved electrical efficiency. Koukharenko et al. [11] studied the mechanical characteristics of the U-shaped micro-generator using the ANSYS software package. More information about the U-shaped structure and its advantages in the literature [12–14].

A double-sided NEMS constructed from a movable cantilever beam suspended between two fixed actuating electrodes. Double-sided NEMS has recently attracted much attention due to its promising electromechanical performance characteristics such as low power consumption, quick response, etc. [15, 16]. The double-sided driven configuration is proposed for the actuation of gyroscopes, microphones, comb drives and memory elements [17, 18]. The double-sided NEMS are also attractive for detecting ultra-small mass, mechanical, electrical, or magnetic forces sensing, biological and chemical sensing, tunable electronics, electromechanical filters, capacitors, switches, etc. [17]. Fu et al. [16] employed the energy balance approach for modeling the oscillation of double-sided microbridges. Khan and Akbarzade employed several analytical methods to study a nonlinear oscillator equation arising in the driven, double-sided, electromechanical resonator [19]. More useful information about double-sided NEMS can be found in Refs. [20, 21].

With recent demands for advanced devices, MEMS/NEMS capacitive sensors are increasingly used in developing precise measurement systems. Measurement of the angular speed has importance in rotary systems, machines and industrial control systems [22]. There are many promising applications such as fault detection of roller bearings [23], balancing power plant rotating equipment [24], measurement of high-speed spindle errors in CNC machining [25], centrifuge devices for separating the solids from liquids [26], etc. Moreover, NEMS can be used as angular speed sensors in turbomachinery. In these applications, the presence of the centrifugal force (the outward pressure on an object rotating around a central point) plays a major role in determining the electromechanical response of the NEMS sensors. Among various types of developed NEMS, the U-shaped and double-sided sensors have been considered as potential capacitive angular speed sensors and accelerometers [27–29]. Herein, the effect of the centrifugal force due to the angular velocity is incorporated into the pull-in models of the U-shaped and double-sided sensors.

To precisely model the aforementioned nanostructures, incorporating the nano-scale phenomena such as the van der Waals (vdW) force is crucial. It is well established that at nano-scale separations (typically less than a few nanometers), the presence of the vdW force substantially affects the pull-in instability of NEMS. Many researchers have investigated the effect of the vdW force on the adhesion and pull-in characteristics of ultra-small systems [30–32]. Wang et al. [32] investigated the nanotube parameters such as the wire radius on the pull-in instability of nanotweezers in the presence of the vdW force. The instability of electromechanical devices due to the vdW force was surveyed by Spengen et al. [33]. Farrokhabadi et al. [34] investigated the static response and pull-in instability of CNT nanotweezers in the presence of the vdW attraction. It should be noted that for large separation the Casimir force should be considered instead of vdW attraction [35, 36]. Herein, the effect of the vdW force is incorporated into our theoretical models.

In addition to the vdW force, the size effect is another crucial phenomenon that should be incorporated into the theoretical modeling of NEMS. Experiments have demonstrated a hardening trend in the elastic behavior of conductive metals and nanowires as the structural dimensions approach the internal material length scale [37, 38]. This size-dependency of material characteristics, i.e. the size effect, cannot be modeled by the classic continuum mechanics. In this regard, the non-classic higher order theories, such as the modified couple stress theory (MCST), are developed to address the size effect in continuum mechanics [39]. The MCST involves only one material length scale parameter to describe the size-dependent behavior of solids. It is simpler in comparison with theories with multiple scale-parameters such as micropolar, strain gradient, etc. The one length scale parameter can be easily determined experimentally or using molecular dynamics methods. Hence, it is more convenience to employ and modeling the size effects. The MCST has been used for investigating the size-dependent pull-in performance of conventional NEMS [40–43]. In the present work, this theory is employed for incorporating the size phenomenon in the governing equations of the systems.

The paper is organized as follows. In Sect. 2, the governing equations of the nanostructures in the vdW regime are derived using the MCST. In Sect. 3, the Duan–Adomian method (DAM) and the differential quadrature method (DQM) are applied to solve these nonlinear equations. Finally, the influences of the centrifugal force, size parameter, vdW attraction and the geometry on the instability voltage and deflection of the nanosystems are demonstrated in Sect. 4.

2 Theory

Figure 1a represents a typical U-shaped sensor made of two nanowires that are connected to a rigid plate. This U-shaped structure is suspended over the fixed plane and can deflect downward by applying an electrostatic attraction between

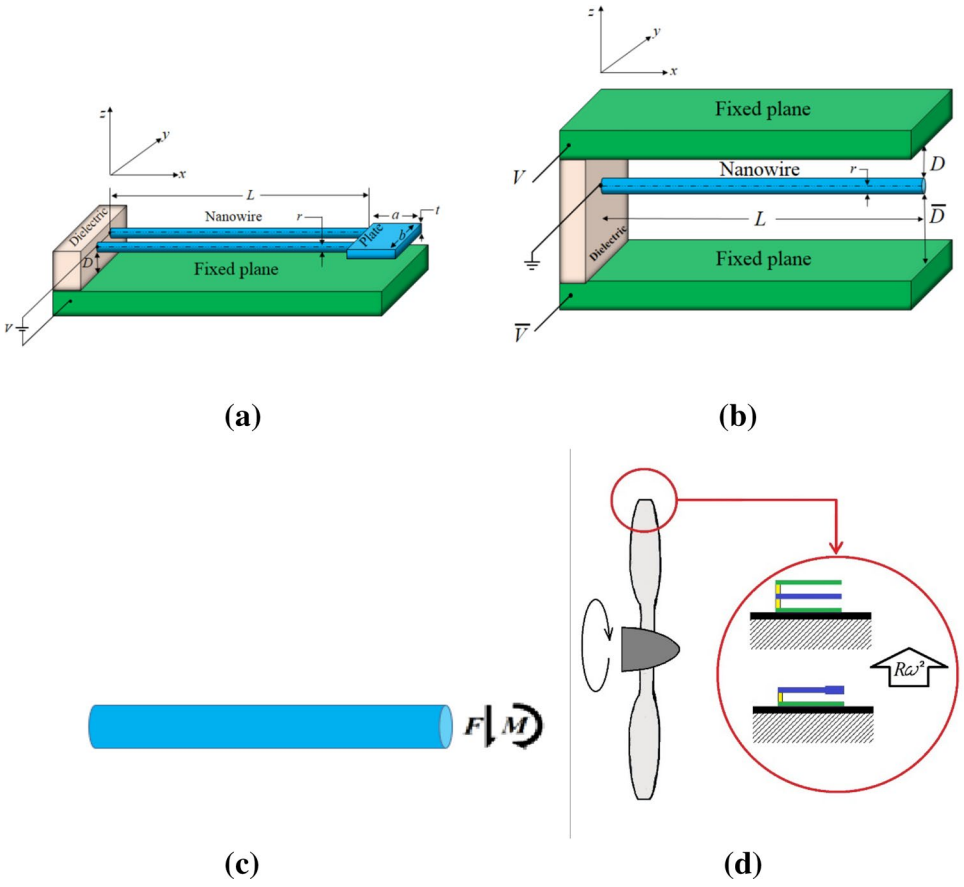

Fig. 1 **a** The schematic representation of the U-shaped NEMS, **b** the schematic representation of the double-sided NEMS, **c** internal resultants in an arbitrary wire cross-section, **d** the nanostructure in the presence of the centrifugal force

the structure and the ground. The DC voltage between the U-shaped structure and the ground plane is V. The nanowire has length L and radius r, and the plate has length a, width b and thickness t.

Figure 1b depicts the schematic of the double-sided sensor fabricated from a movable cantilever nanowire suspended between two fixed plane electrodes. The DC voltage difference and initial gap between the movable electrode and upper plane are V and D, respectively. The potential difference and initial separation between the nanowire and the lower ground plane are $\bar{V}$ and $\bar{D}$, respectively. The nanowire has length L and radius r. The nanowire can deflect up or down towards either of the fixed planes depending on the actuation force.

The structural resultants in an arbitrary wire cross-section are shown in Fig. 1c. In this figure, F and M denote the internal force and moment at the non-supported end of the nanowire (at $x = L$), respectively.

Now consider the double-sided and U-type sensors in the presence of the centrifugal force as shown in Fig. 1d. To obtain the equation of motion of the nanowire, Hamilton's principle is applied to yield the equilibrium for the minimum value of free energy as

$$\delta(U - V) = 0, \tag{1}$$

where δ denotes the variation symbol, U is the strain energy and V is the work done by all forces.

2.1 Strain energy

To compute the strain energy of the system, the size-dependent MCST is used. According to this theory [39], the strain energy density can be expressed as [39]

$$\tilde{u} = \frac{1}{2}\left(\sigma_{ij}\varepsilon_{ij} + m_{ij}\chi_{ij}\right), \quad (i,j = 1,2,3), \tag{2}$$

where the variables σ_{ij}, ε_{ij}, m_{ij} and χ_{ij} are the stress tensor, strain tensor, deviatoric part of the couple stress tensor and symmetric part of the curvature tensor, respectively. These tensors are determined from the following relations:

$$\sigma_{ij} = \lambda\varepsilon_{mm}\delta_{ij} + 2\mu\varepsilon_{ij}, \tag{3a}$$

$$\varepsilon_{ij} = \frac{1}{2}\left((\nabla u)_{ij} + (\nabla u)_{ij}^{\mathrm{T}}\right), \tag{3b}$$

$$m_{ij} = 2l^2\mu\chi_{ij}, \tag{3c}$$

$$\chi_{ij} = \frac{1}{2}\left((\nabla\theta)_{ij} + (\nabla\theta)_{ij}^{\mathrm{T}}\right), \tag{3d}$$

$$\theta_i = \frac{1}{2}(\nabla \times u)_i, \tag{3e}$$

where λ, μ and l are the Lamé constant, shear modulus and the material length scale parameter, respectively. Also, u and θ are the displacement and rotation vectors, respectively.

According to the Euler–Bernoulli beam model, the displacement components for the nanowire is assumed as [44]

$$u = -z\frac{\partial w(X)}{\partial X}, \quad v = 0, \quad w = w(X). \tag{4}$$

Since the pull-in instability often happens at small values of deflections, hence to reduce the complexity of mathematical model, a small displacement assumption is used [45]. Indeed, comparison between the large and small displacement models shows that small-deflection assumption produce precise enough results for modeling the pull-in instability of cantilever-type systems with low values of the gap to length ratio [45]. This is common case in fabrication of the cantilever-type systems.

By substitution of Eqs. (3) and (4) into relations (2), the following expressions for the main components of the strain and stress tensors are obtained as

$$\chi_{xy} = -\frac{1}{2}\frac{\partial^2 w}{\partial X^2}, \quad \chi_{XX} = \chi_{YY} = \chi_{ZZ} = \chi_{YZ} = \chi_{ZX} = 0, \tag{5a}$$

$$m_{xy} = -\mu l^2\frac{\partial^2 w}{\partial X^2}, \quad m_{XX} = m_{YY} = m_{ZZ} = m_{YZ} = m_{XZ} = 0, \tag{5b}$$

$$\varepsilon_{xx} = -z\frac{\partial^2 w}{\partial X^2}, \quad \varepsilon_{YY} = \varepsilon_{ZZ} = \varepsilon_{XY} = \varepsilon_{YZ} = \varepsilon_{ZX} = 0, \tag{5c}$$

$$\sigma_{xx} = -E_{\mathrm{eff}}z\frac{\partial^2 w}{\partial X^2}, \quad \sigma_{YY} = \sigma_{ZZ} = \sigma_{YZ} = \sigma_{ZX} = \sigma_{XY} = 0, \tag{5d}$$

where E_{eff} is Young's modulus.

By substituting Eqs. (5a–5d) into Eq. (2), and integrating over the length of the nanowire, we can obtain the relation for the strain energy in Eq. (1) as

$$U = \frac{1}{2}\int_0^L \left(E_{\mathrm{eff}}I + \mu A l^2\right)\left(\frac{\partial^2 w}{\partial X^2}\right)^2 \mathrm{d}X, \tag{6}$$

where I is the second moment of the cross-sectional area around the Y axis and A is the cross-sectional area of the nanowire.

2.2 Work by all forces

The work by all forces in Eq. (1) can be determined by considering the free-body diagram of the nanowire (Fig. 1c). The work by all forces is the summation of the work done by the external forces (f_{ext}) and the work done by the tractions at the non-supported wire end, i.e. the internal moment (M) and force (F).

The external forces include the electrostatic and vdW attractions. The work done by the external forces, $V_{f_{\mathrm{ext}}}$, can be written as

$$V_{f_{\mathrm{ext}}} = \int_0^L \int_0^w f_{\mathrm{ext}}\mathrm{d}w\mathrm{d}X. \tag{7}$$

The work done by the internal moment, V_{M}, is obtained as

$$V_M = \int_0^{\frac{\partial w(L)}{\partial X}} M\left(w(L), \frac{\partial w(L)}{\partial X}\right) \times d\frac{\partial w(L)}{\partial X}. \tag{8}$$

The work done by the internal force, V_{F}, is determined as

$$V_{\mathrm{F}} = \int_0^{w(L)} F\left(w(L), \frac{\partial w(L)}{\partial X}\right) \times dw(L). \tag{9}$$

Finally, the overall work done by the aforementioned forces is obtained as

$$V = V_{f_{\mathrm{ext}}} + V_{\mathrm{M}} + V_{\mathrm{F}} = \int_0^L \int_0^w f_{\mathrm{ext}}\mathrm{d}Z\mathrm{d}X + \int_0^{\frac{\partial w(L)}{\partial X}} M\left(w(L), \frac{\partial w(L)}{\partial X}\right) \times d\frac{\partial w(L)}{\partial X} + \int_0^{w(L)} F\left(w(L), \frac{\partial w(L)}{\partial X}\right) \times dw(L). \tag{10}$$

2.3 Governing equation

By substituting relations (6) and (10) into (1), we can obtain the variation as

$$\delta(V-U)=\int_0^L\left[\left(E_{\text{eff}}I+\mu Al^2\right)\frac{\partial^4 w}{\partial X^4}-f_{\text{ext}}\right]\delta w\mathrm{d}X - \left(E_{\text{eff}}I+\mu Al^2\right)\frac{\partial^3 w}{\partial X^3}\delta w\Big|_0^L + \left(E_{\text{eff}}I+\mu Al^2\right)\frac{\partial^2 w}{\partial X^2}\delta\left(\frac{\partial w}{\partial X}\right)\Big|_0^L - M\delta\left(\frac{\partial w}{\partial X}\right)\Big|_L - F\delta w|_L=0. \tag{11}$$

Hence, the governing equation for the equilibrium of the nanowire is derived from Eq. (11) as

$$\left(E_{\text{eff}}I+\mu Al^2\right)\frac{\mathrm{d}^4 w}{\mathrm{d}X^4}=f_{\text{ext}} \tag{12a}$$

with the following geometric boundary conditions

$$w(0)=0,\quad \frac{\mathrm{d}w}{\mathrm{d}X}(0)=0, \tag{12b}$$

and the following natural boundary conditions

$$\left(E_{\text{eff}}I+\mu Al^2\right)\frac{\mathrm{d}^2 w}{\mathrm{d}X^2}(L)=M,\quad \left(E_{\text{eff}}I+\mu Al^2\right)\frac{\mathrm{d}^3 w}{\mathrm{d}X^3}(L)=-F. \tag{12c}$$

We emphasize that Eqs. (12b) and (12c) imply zero displacement at the clamped end as well as the force and moment balances at the non-supported end of the wire(s). The relation of Eq. (12) can be more specialized for each sensor by defining f_{ext}, M and F. This is accomplished in the subsequent subsections.

2.3.1 U-shaped structure

For each beam element of the U-shaped sensor (Fig. 1a), the f_{ext} in Eq. (12) is the summation of the electrostatic, vdW and centrifugal forces per unit length of the nanowire. Thus, f_{ext} can be defined as

$$f_{\text{ext}}=f_{\text{elec}}+f_{\text{vdW}}+f_{\text{Rot}}, \tag{13}$$

where f_{elec}, f_{vdW} and f_{Rot} are the electrostatic, vdW and centrifugal forces, respectively. The electrostatic force terms in relation (12) can be determined from the capacitive model [46]. Based on capacitive model, the electrostatic energy for a cylindrical conductor parallel to a conductive plane (E_{elec}) is given as [47]

$$E_{\text{elec}}=\frac{\pi\varepsilon_0\varepsilon_r LV^2}{\operatorname{arccosh}\left(1+\frac{D}{r}\right)}, \tag{14}$$

where ε_0 and V are the permittivity of vacuum and the applied voltage, respectively. Hence, by differentiating the electrostatic energy, the electrostatic force per unit length of the cylinder, f_{elec}, can be obtained from Eq. (14) as

$$f_{\text{elec}}=\frac{\pi\varepsilon_0\varepsilon_r V^2}{\sqrt{(D+2r)(D)}\operatorname{arccosh}^2\left(1+\frac{D}{r}\right)}. \tag{15}$$

The vdW energy between a cylinder and a flat plane can be evaluated as [48]

$$E_{\text{vdW}}=-\frac{HL}{12}\sqrt{\frac{r}{2D^3}}, \tag{16}$$

where H is the Hamaker constant. Therefore, the vdW force per unit length of the nanowire, f_{vdW}, is derived by differentiating the energy as

$$f_{\text{vdW}}=\frac{H}{8}\sqrt{\frac{r}{2D^5}}, \tag{17}$$

According to D'Alembert's principal, we can transform an angular speed into an equivalent centrifugal force. Hence, the contribution of the centrifugal force can be modeled by considering the angular velocity of the system. The centrifugal force per unit length of the nanowire, caused by rotation of a rotary machine, is determined as [28, 29]

$$f_{\text{Rot}}=\pi\rho r^2(R\pm D)\omega^2, \tag{18}$$

where ρ, R, and ω are the density of the nanowire, the rotary surface radius and the angular speed of the rotary surface, respectively. For the case of $R\gg D$, Eq. (18) reduces to

$$f_{\text{Rot}}=\pi\rho r^2 R\omega^2. \tag{19}$$

By replacing D with D–w in relations (15), (17) and using Eq. (19), f_{ext} can be defined as

$$f_{\text{ext}}=f_{\text{elec}}+f_{\text{vdW}}+f_{\text{Rot}}=\frac{\pi\varepsilon_0\varepsilon_r V^2}{\sqrt{(D-w+2r)(D-w)}\operatorname{arccosh}^2\left(1+\frac{D-w}{r}\right)}+\frac{H}{8}\sqrt{\frac{r}{2(D-w)^5}}+\pi\rho r^2 R\omega^2. \tag{20}$$

For the U-shaped sensor, the stress resultants F and M are induced by the electrostatic, vdW and centrifugal forces acting on the rigid plate. The exact value of F and M can be calculated in the form of a complex function of the dominant parameters; see Appendix. Substituting the exact values of F and M into Eq. (12c) results in a nonlinear differential equation subject to highly complex boundary conditions. Unfortunately, this complex equation cannot be easily solved using analytical methods. Therefore, a simplification of F and M is required to achieve an analytically solvable equation for the U-shaped system, while retaining most of the significant effects.

To obtain a set of appropriate boundary conditions, the distributed forces acting on the rigid plate are replaced with an equivalent concentrated force acting at a distance $\bar{x}$ from the nanowire tip (the force center). The value of $\bar{x}$ is determined from the $\bar{x} = M/F$ relation. The details of the approach and its validity are presented in Appendix. Based on this approach, the boundary conditions in the non-supported wire end can be obtained as

$$(E_{\text{eff}}I + \mu Al2)\frac{\mathrm{d}^2 w}{\mathrm{d}X^2}(L) = \frac{\varepsilon_0\varepsilon_r}{4}\frac{abV^2\bar{x}}{(D - w(L) - \bar{x}w'(L))^2} + \frac{Hab\bar{x}}{12\pi(D - w(L) - \bar{x}w'(L))^3} + \frac{\rho a^2 btR\omega^2}{4}, \tag{21a}$$

$$(E_{\text{eff}}I + \mu Al2)\frac{\mathrm{d}^3 w}{\mathrm{d}X^3}(L) = \frac{\varepsilon_0\varepsilon_r}{4}\frac{abV^2}{(D - w(L) - \bar{x}w'(L))^2} + \frac{Hab}{12\pi(D - w(L) - \bar{x}w'(L))^3} - \frac{\rho abtR\omega^2}{2}. \tag{21b}$$

By substituting Eqs. (20) and (21) into (12), the nondimensional governing equation of the U-shaped sensor can be written as

$$(1+\delta)\frac{\mathrm{d}^4\hat{w}}{\mathrm{d}x^4} = \frac{\beta}{\sqrt{(1-\hat{w})\left[1+k(1-\hat{w})\right]}\operatorname{arccosh}^2\left(1+2k(1-\hat{w})\right)} + \frac{\alpha}{(1-\hat{w})^{\frac{5}{2}}} + \bar{\omega}, \tag{22a}$$

$$\hat{w}(0) = \hat{w}'(0) = 0, \tag{22b}$$

$$(1+\delta)\frac{\mathrm{d}^2\hat{w}}{\mathrm{d}x^2}(1) = \vartheta\Omega\xi\tau\left[\frac{\beta}{2k^{\frac{3}{2}}(1-\hat{w}(1)-\Omega\xi\tau\hat{w}'(1))^2} + \frac{8\alpha}{3k^{\frac{1}{2}}(1-\hat{w}(1)-\Omega\xi\tau\hat{w}'(1))^3} + \frac{2\bar{\omega}}{\Omega}\right], \tag{22c}$$

$$(1+\delta)\frac{\mathrm{d}^3\hat{w}}{\mathrm{d}x^3}(1) = -\vartheta\left[\frac{\beta}{2k^{\frac{3}{2}}(1-\hat{w}(1)-\Omega\xi\tau\hat{w}'(1))^2} + \frac{8\alpha}{3k^{\frac{1}{2}}(1-\hat{w}(1)-\Omega\xi\tau\hat{w}'(1))^3} + 4\bar{\omega}\right]. \tag{22d}$$

In Eq. (22), the following dimensionless parameters defined as

$$\begin{aligned} &x = \frac{X}{L},\ \hat{w}\frac{w}{D},\ \xi = \frac{a}{D},\ \tau = \frac{D}{L},\ k = \frac{D}{2r},\\ &\delta = \frac{\mu Al^2}{E_{\text{eff}}I} = \frac{4\mu l^2}{E_{\text{eff}}r^2},\ \upsilon = \frac{ab}{4\pi rL},\\ &\Omega = \frac{\bar{x}}{a},\ \alpha = \frac{Hr^{\frac{1}{2}}L^4}{8\sqrt{2}E_{\text{eff}}ID^{\frac{7}{2}}},\ \beta = \frac{\varepsilon_0\varepsilon_r\pi V^2K^4}{\sqrt{2}r^{\frac{1}{2}}E_{\text{eff}}ID^{\frac{3}{2}}},\\ &\bar{\omega} = \frac{\pi\rho r^2L^4R\omega^2}{E_{\text{eff}}ID}. \end{aligned} \tag{23}$$

2.3.2 Double-sided structure

For the double-sided sensor (Fig. 1b), the f_{ext} in Eq. (12) is the summation of the electrostatic, vdW and centrifugal forces per unit length of the nanowire by considering the effects of both upper and lower fixed electrodes. Thus, f_{ext} can be defined as

$$f_{ext} = f_{elec1} - f_{elec2} + f_{vdW1} - f_{vdW2} + f_{Rot}, \tag{24}$$

where f_{elec1} and f_{vdW1} are the electrostatic and vdW forces between the wire and the upper plane, respectively. f_{elec2} and f_{vdW2}, denote the electrostatic and vdW forces between the wire and the lower plane, respectively. By considering the deflection of the nanowire and replacing D with D–w in Eqs. (15) and (17), f_{elec1} and f_{vdW1} can be derived. Similarly f_{elec2} and f_{vdW2} can be obtained by substituting D with $\xi D + w$ in relations (15) and (17). The boundary conditions for the double-sided sensor are defined as traction free at the free end ($F = M = 0$). Hence, Eq. (12c) is reduced to the following relations

$$\frac{d^2 w}{dX^2}(L) = \frac{d^3 w}{dX^3}(L) = 0. \tag{25}$$

For the double-sided sensor, by using Eqs. (15), (17), (19) and (22), the governing equation of (12) can be finally written as

$$(1+\delta)\frac{d^4\hat{w}}{dx^4} = \frac{\beta}{\sqrt{(1-\hat{w})[1+k(1-\hat{w})]}\operatorname{arccosh}^2(1+2k(1-\hat{w}))} - \frac{\eta\beta}{\sqrt{(\xi+\hat{w})[1+k(\xi+\hat{w})]}\operatorname{arccosh}^2(1+2k(\xi+\hat{w}))} + \frac{\alpha}{(1-\hat{w})^{\frac{5}{2}}} - \frac{\alpha}{(\xi+\hat{w})^{\frac{5}{2}}} + \bar{\omega}, \tag{26a}$$

$$\hat{w}(0) = \frac{d\hat{w}}{dx}(0), \tag{26b}$$

$$\frac{d^2\hat{w}}{dx^2}(1) = \frac{d^3\hat{w}}{dx^3}(1) = 0. \tag{26c}$$

where the dimensionless parameters are defined as

$$\xi = \frac{\bar{D}}{D}, \quad \eta = \left(\frac{\bar{V}}{V}\right)^2. \tag{27a}$$

3 Solution methods

3.1 Duan–Adomian method (DAM)

Recently, Duan [49] has developed a fast decomposition algorithm that is employed in conjunction with the Adomian decomposition method [50] in solving higher order boundary value problems. To analytically solve the governing equation of the systems Eqs. (22) and (26), we consider the following general form of the fourth-order differential equation with the nonlinearity $f(x, \hat{w})$ as

$$\frac{d^4\hat{w}(x)}{dx^4} = f(x, \hat{w}(x)), \tag{28a}$$

$$\hat{w}(0) = C_1, \quad \hat{w}'(0) = C_2. \tag{28b}$$

The solution of Eq. (28a) can be determined as

$$\hat{w}(x) = \sum_{k=1}^{\infty}\hat{w}_n(x) = C_1 + C_2 x + \frac{1}{2!}C_3 x^2 + \frac{1}{3!}C_4 x^3 + \int_0^x\int_0^x\int_0^x\int_0^x \left(\left[\sum_{n=0}^{\infty} f_n(x)\right]\right) dx\,dx\,dx\,dx, \tag{29}$$

where C_1, C_2, C_3 and C_4 are the constants of integration. Note that in the case of Eq. (12), the values of C_1 and C_2 are both zero. Based on the DAM, the polynomials $f_n(x)$ are determined from the following relation [49, 51] as

$$f_n = \sum_{k=1}^{n} C_n^k h^{(k)}(\hat{w}_0), \tag{30}$$

where the derivative terms, $h^{(k)}$, and the coefficients, C_n^k, satisfy the following recurrence algorithm:

$$C_n^k = \begin{cases} \hat{w}_n, & k = 1, n \geq 1, \\ \frac{1}{n}\sum_{j=0}^{n-k}(j+1)\hat{w}_{j+1}C_{n-1-j}^{k-1}, & 2 \leq k \leq n, \end{cases} \tag{31a}$$

$$h^{(k)} = \frac{\partial^k f}{\partial \hat{w}_0^k}, \quad k \geq 1. \tag{31b}$$

Now, by using relations (29) and (30), the solution of Eq. (22) can be presented as

$$\hat{w} = \frac{1}{2!}C_3x^2 + \frac{1}{3!}C_4x^3 + \frac{1}{4!(1+\delta)}\left[\frac{\beta}{\sqrt{1+k}\arccos h^2(1+2k)} + \alpha + \bar{\omega}\right]x^4 + \frac{1}{7!(1+\delta)}\left[\frac{2\beta\sqrt{k}}{(1+k)\arccos h^3(1+2k)} + \frac{\beta(1+2k)}{2(1+k)^{3/2}\arccos h^2(1+2k)} + \frac{5\alpha}{2}\right]\left[7C_3x^6 + C_4x^7\right] + \cdots. \tag{32}$$

Similarly, the solution of Eq. (26) can be determined as

$$\hat{w} = \frac{1}{2!}C_3x^2 + \frac{1}{3!}C_4x^3 + \frac{1}{4!(1+\delta)}\left[\frac{\beta}{\sqrt{1+k}\text{arccosh}^2(1+2k)} - \frac{\beta\eta}{\sqrt{\xi(1+k\xi)}\text{arccosh}^2(1+2k\xi)} + \alpha - \frac{\alpha}{\sqrt{\xi^5}} + \bar{\omega}\right]x^4 + \frac{1}{7!(1+\delta)}\left[\frac{2\beta\sqrt{k}}{(1+k)\text{arccosh}^3(1+2k)} + \frac{2\beta\sqrt{k}\eta}{\xi(1+k\xi)\text{arccosh}^3(1+2k\xi)} + \frac{\beta(1+2k)}{2(1+k)^{3/2}\text{arccosh}^2(1+2k)} + \frac{\beta\eta(1+2k\xi)}{2\sqrt{\xi^3}(1+k\xi)^{3/2}\text{arccosh}^2(1+2k\xi)} + \frac{5\alpha}{2} + \frac{5\alpha}{2\sqrt{\xi^7}}\right]\left[7C_3x^6 + C_4x^7\right] + \cdots. \tag{33}$$

Finally, the constants C_3 and C_4 are obtained from the boundary conditions of (22b, c, d) and (26b, c) for the U-shaped and double-sided nanostructures, respectively.

3.2 Differential quadrature method (DQM)

To solve Eqs. (22) and (26) by the DQM, the nanowire is discretized into $N-1$ segments separated by N nodes. In the DQM method, the rth-order derivatives of the function $f(x)$ defined as [52]

$$\left.\frac{\partial^r f}{\partial x^r}\right|_{x=x_i} = \sum_{j=1}^{N} A_{ij}^{(r)} f(x_j), \tag{34}$$

where the weighed coefficient of rth-order derivatives are defined as

$$A_{ij}^{1} = \frac{M(x_i)}{(x_i - x_j)(M_{X_j})} \quad (i,j = 1,2,\ldots,N; i \neq j),$$
$$A_{ij}^{(r)} = \begin{cases} r\left[A_{ij}^{(r-1)}A_{ij}^{(r)} - \dfrac{A_{ij}^{(r-1)}}{x_i - x_j}\right], & i \neq j \\ -\displaystyle\sum_{j=1}^{N} A_{ij}, & i = j (i,j = 1,2,\ldots,N; 2 \leq r \leq N-1), \end{cases} \tag{35}$$

where

$$M(x_i) = \prod_{j=1;j\neq i}^{N} (x_i - x_j). \tag{36}$$

The sample points of the discrete domain are obtained from the Chebyshev–Gauss–Lobatto nodal point formula as [52]

$$x_i = \frac{L}{2}\left(1 - \cos\frac{i-1}{N-1}\pi\right), \quad i = 1,2,3,\ldots,N. \tag{37}$$

Now, by using Eqs. (35–37), the solution of Eq. (22) is obtained as

$$(1+\delta)\sum_{j=1}^{N} A_{ij}^{(4)}\hat{w}_j = \frac{\beta}{\sqrt{(1-\hat{w})[1+k(1-\hat{w})]}\arccos h^2(1+2k(1-\hat{w}))} + \frac{\alpha}{(1-\hat{w})^{\frac{5}{2}}} + \bar{\omega}, \tag{38a}$$

$$\hat{w}_1\sum_{j=1}^{N} A_{1j}^{(1)}\hat{w}_j = 0, \tag{38b}$$

$$(1+\delta)\sum_{j=1}^{N} A_{Nj}^{(2)}\hat{w}_j = \vartheta\Omega\xi\tau\left[\frac{\beta}{2k^{\frac{3}{2}}(1-\hat{w}_N - \Omega\xi\tau\sum_{j=1}^{N} A_{Nj}^{(1)}\hat{w}_j)^2} + \frac{8\alpha}{3k^{\frac{1}{2}}(1-\hat{w}_N - \Omega\xi\tau\sum_{j=1}^{N} A_{Nj}^{(1)}\hat{w}_j)^3} + \frac{2\bar{\omega}}{\Omega}\right], \tag{38c}$$

$$(1+\delta)\sum_{j=1}^{N} A_{Nj}^{(3)}\hat{w}_j = -\vartheta\left[\frac{\beta}{2k^{\frac{3}{2}}(1-\hat{w}_N - \Omega\xi\tau\sum_{j=1}^{N} A_{Nj}^{(1)}\hat{w}_j)^2} + \frac{8\alpha}{3k^{\frac{1}{2}}(1-\hat{w}_N - \Omega\xi\tau\sum_{j=1}^{N} A_{Nj}^{(1)}\hat{w}_j)^3} + 4\bar{\omega}\right]. \tag{38d}$$

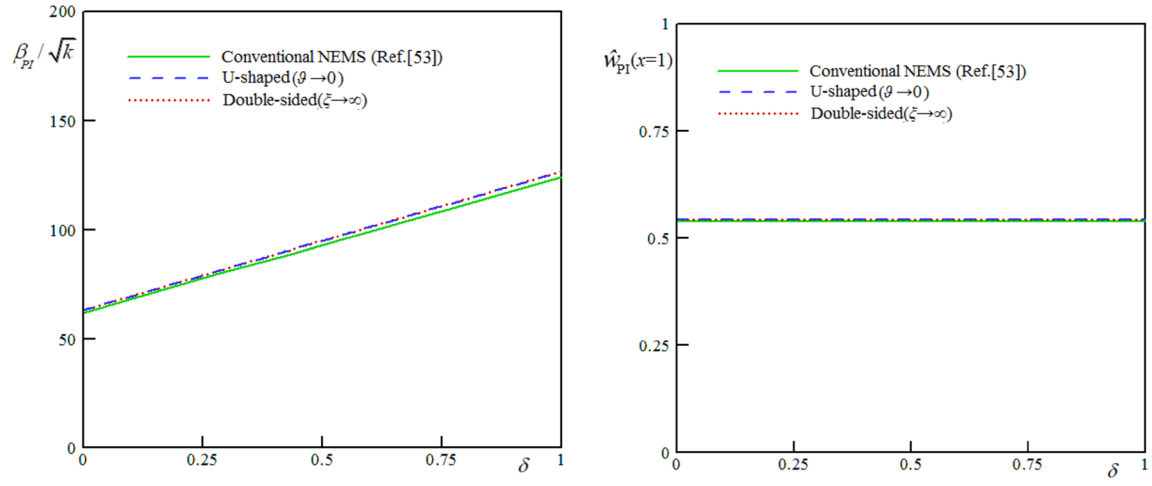

Fig. 2 Effect of the size dependence on the pull-in characteristics. Comparison between the conventional, asymptotic U-shaped ($\vartheta \to 0$) and asymptotic double-sided ($\xi \to \infty$) systems using $D/R = 100$, $\alpha = 0$ and $\bar{\omega} = 0$; **a** pull-in voltage, **b** pull-in deflection

Similarly, the solution of Eq. (26) is obtained as

$$(1+\delta)\sum_{j=1}^{N} A_{ij}^{(4)}\hat{w}_j = \frac{\beta}{\sqrt{(1-\hat{w}_i)[1+k(1-\hat{w}_i)]}\arccosh^2(1+2k(1-\hat{w}_i))} - \frac{\eta\beta}{\sqrt{(\xi-\hat{w}_i)[1+k(\xi-\hat{w}_i)]}\arccosh^2(1+2k(\xi-\hat{w}_i))} + \frac{\alpha}{(1-\hat{w})^{\frac{5}{2}}} - \frac{\alpha}{(\xi-\hat{w}_i)^{\frac{5}{2}}} + \bar{\omega}, \tag{39a}$$

$$\hat{w}_1 \sum_{j=1}^{N} A_{1j}^{(1)}\hat{w}_j = 0, \tag{39b}$$

$$\sum_{j=1}^{N} A_{Nj}^{(2)}\hat{w}_j = \sum_{ij}^{N} A_{Nj}^{(3)}\hat{w}_j = 0. \tag{39c}$$

The above algebraic systems of Eqs. (38) and (39) are then numerically solved and the nodal deflections are determined. When the instability occurs, no solution exists for Eqs. (38) and (39) and thus the pull-in instability parameters of the nanostructures are obtained by plotting the NEMS tip deflection versus the applied force.

4 Results and discussion

4.1 Validation

To validate the proposed approaches, the asymptotic limits of the theoretical models of the U-shaped and double-sided

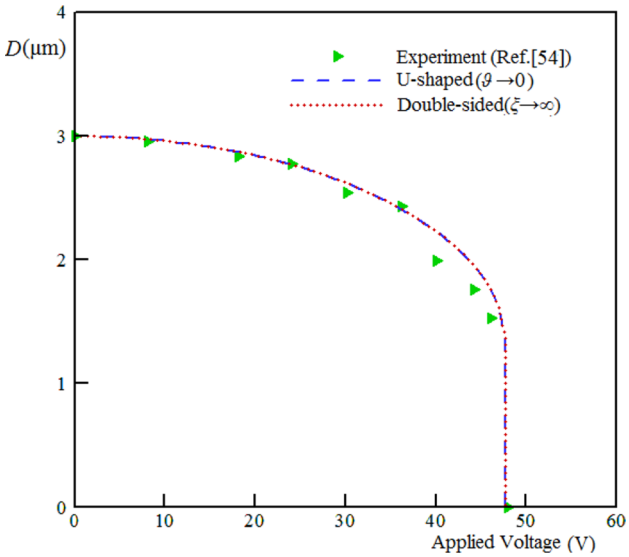

Fig. 3 Comparison between the instability voltages determined by the developed models and by experiment [54]. $E_{\text{eff}} = 0.9$ TPa, $D = 3$ μm and $R = 23.5$ nm

sensors (Eqs. 22, 26) are compared with the conventional nanostructure as presented in Ref. [53]. The conventional system is made of a cantilever nanowire with a circular cross-section suspended over the ground plane [53]. Figure 2 presents the variation of the pull-in characteristics of the nanowire versus the size effect parameter for a typical conventional [53], asymptotic U-shaped ($\vartheta \to 0$) and asymptotic double-sided ($\xi \to \infty$) systems. It can be shown that if $\vartheta \to 0$, then the results of Eq. (22) (U-shaped) approaches those of the conventional cantilever system. Similar results can be obtained from Eq. (26) (double-sided) as $\xi \to \infty$.

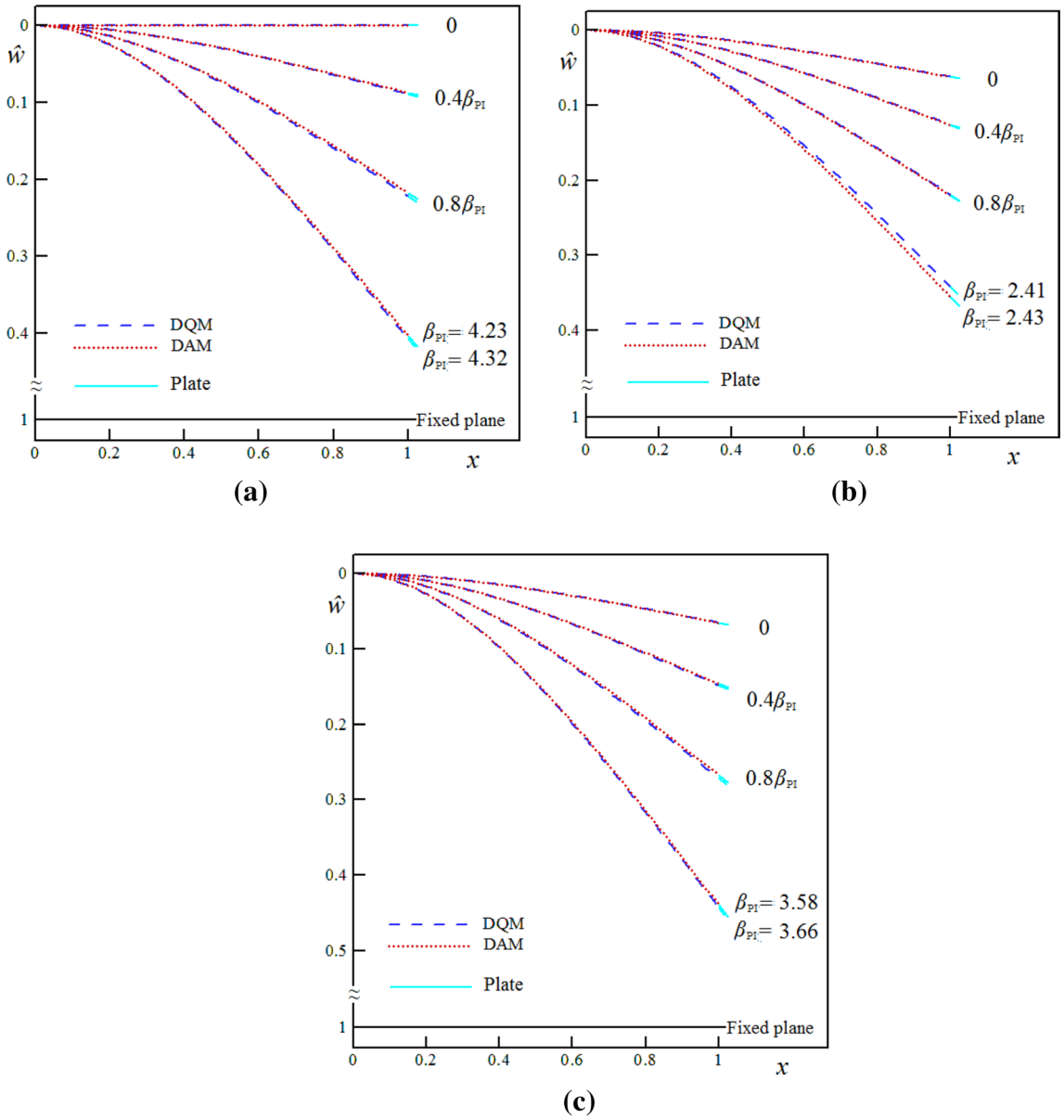

Fig. 4 Displacement of the nanowires for different values of β. $k = 1$, $\xi = 0.5$, $\tau = 0.05$, $\vartheta = 0.1$, $\Omega = 0.5$, $\bar{\omega} = 0$ and $\delta = 0$; **a** no vdW and centrifugal forces, **b** considering the vdW force and no centrifugal force ($\alpha = 0.25$, $\bar{\omega} = 0$), **c** considering the centrifugal force and no vdW force ($\bar{\omega} = 0.25$, $\alpha = 0$)

Furthermore, the validity of the present model is examined by comparing the theoretical values in the asymptotic limit ($\vartheta \to 0$, $\xi \to \infty$) with the experimental measurements as reported in the literature. Ke et al. [54] measured the instability voltage of the carbon-fabricated probe. The comparison between the pull-in voltages, as calculated using the present models and as measured by Ke et al. [54], is depicted in Fig. 3. As shown, an acceptable agreement between the theories and experiment are observed that corroborates the validity of the proposed models in modeling the pull-in instability.

4.2 U-shaped sensors

The electromechanical behavior of a typical cantilever U-shaped nanosensor is presented in Fig. 4. Figure 4a demonstrates the trend of the nanowire deflection in the absence of the vdW and centrifugal forces ($\alpha = \bar{\omega} = 0$).

Figure 4b shows the deflection of the wire in the presence of the vdW force but in the absence of the centrifugal force ($\bar{\omega} = 0$, $\alpha = 0.25$). Figure 4c depicts the centerline deflection of the sensor in the absence of the vdW force but with a positive value of the centrifugal force ($\bar{\omega} = 0.25$, $\alpha = 0$). As shown from these figures, a positive value of the centrifugal force decreases the pull-in voltage while slightly increasing the pull-in deflection of the sensor.

The relation between $\hat{w}_{\text{tip}}$ and β is displayed in Fig. 5. As shown from this figure, the vdW force decreases the pull-in voltage and pull-in deflection of the sensor. If the separation between the nanowire(s) and the plane becomes sufficiently large (micro-scale), the electrostatic force predominates and the vdW force can be neglected. However, the combined effects of the electrostatic and vdW forces should be taken into account if the gap is of the order of several nanometers.

Figure 6 presents the pull-in voltage of the sensor as a function of the centrifugal force. This figure shows that for positive values of the centrifugal force, the pull-in voltage decreases as the angular speed increases. On the other hand, for negative values of the centrifugal force, an increase in the angular velocity increases the instability threshold of the systems.

To exhibit the effect of the rigid plate geometry on the stability of the U-shaped sensor, the variation of the pull-in voltage as a function of the geometric parameter ϑ is plotted in Fig. 7. The geometric parameter ϑ represents the ratio between the plate surface area to the nanowire surface area. It can be shown that the pull-in voltage (β_{PI}) decreases with increasing ϑ. This implies that an increase in the plate surface increases the external forces and decreases the stability threshold of the sensor. Moreover, Fig. 6 shows that the effect of the vdW force on the instability is more pronounced for larger values of ϑ.

Figure 8 displays the effect of the size phenomenon on the pull-in performance of the U-shaped sensor. The effect of the size phenomenon should be incorporated for precise modeling of the sensors fabricated from size-dependent materials such as conductive metals [37, 38]. As shown in this figure, an increase in the size parameter (δ) increases the instability voltage of the sensor. Furthermore, this figure shows that the effect of the size phenomenon on the instability of the U-shaped nanostructure is more pronounced for higher values of ϑ (large plates).

For a freestanding sensor, i.e. no Coulomb attraction, when the vdW parameter α exceeds the critical value (α_{cr}), no solution exists for the wire(s) deflection, i.e. the wire(s) collapses onto and adheres to the fixed ground. The maximum permissible length of the nanowire, L_{max}, to avoid the adherence is crucial in the design and fabrication of miniature sensors [44, 55]. The value of L_{max} can be determined

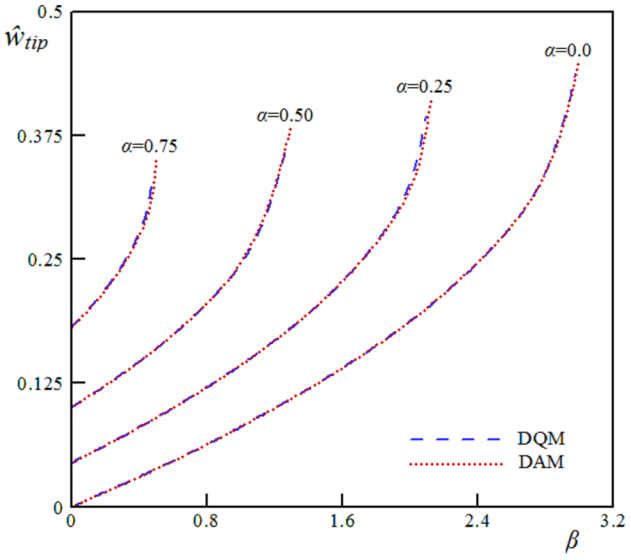

Fig. 5 The tip deflection of the nanowires versus β for different values *of* α ($k = 0.5$, $\xi = 0.3$, $\tau = 0.02$, $\vartheta = 0.03$, $\Omega = 0.5$, $\bar{\omega} = 0$ and $\delta = 0$)

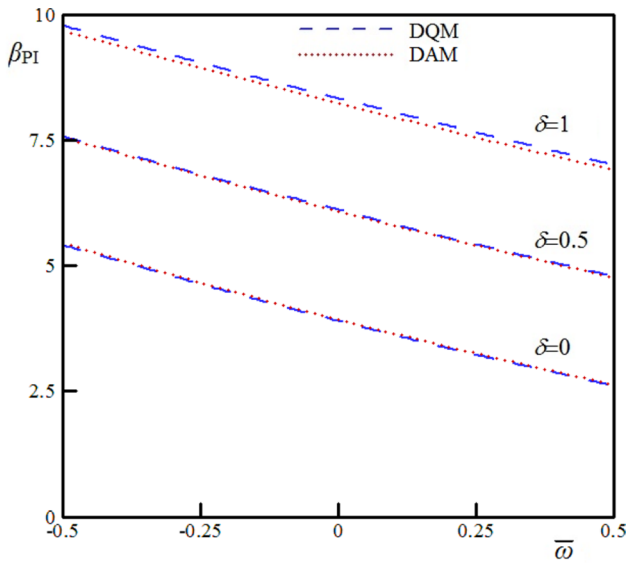

Fig. 6 The variation of β_{PI} versus $\bar{\omega}$ for different δ values ($k = 1$, $\xi = 0.3$, $\tau = 0.02$, $\Omega = 0.5$, $\vartheta = 0.1$ and $\alpha = 0.05$)

by computing α_{cr} (by considering $\beta = 0$ and solving Eq. (22) for the U-shaped structure), and then substituting α_{cr} into the definition of α (Eq. 23). The variation of L_{max} for a typical freestanding U-shaped graphite sensor as a function of the nanowire radius and initial gap is shown in Fig. 9 in the absence of the centrifugal force. As shown, increasing the gap and diameter of the nanowire leads to a significant increase in the maximum permissible length of the wires.

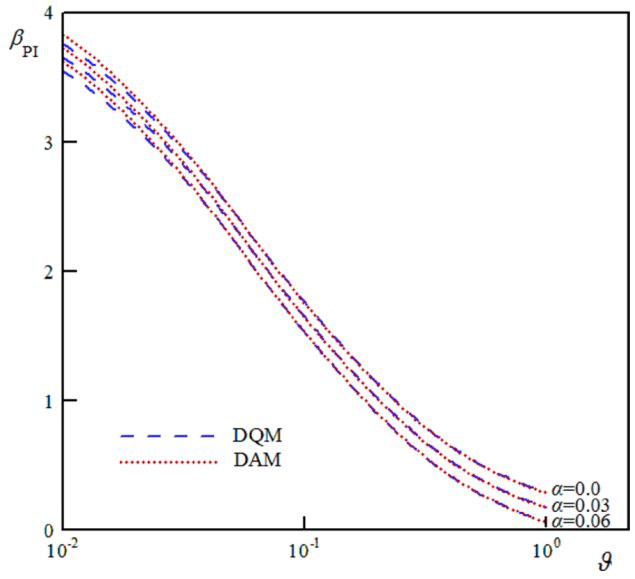

Fig. 7 The variation of the pull-in voltage versus ϑ for different values of α ($k = 0.5$, $\xi = 0.3$, $\tau = 0.02$, $\Omega = 0.5$, $\bar{\omega} = 0$ and $\delta = 0$)

Similarly, the variation of L_{max} for a typical freestanding U-shaped graphite sensor as a function of the rotary surface radius and the angular speed of the rotary surface is shown in Fig. 10. The values of $R = 5$ cm, $R = 0.5$ m and $R = 5$ m corresponds to the radii of a typical centrifuge rotor, an airplane propeller and a helicopter blade, respectively. According to Fig. 10, for a small separation ($D = 10$ nm), the angular speed of rotary surface does not substantially affect the value of L_{max} of the nanowire. While, at larger

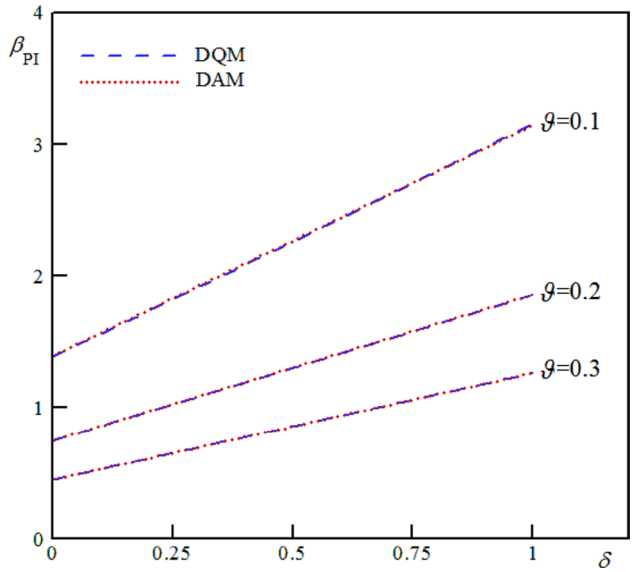

Fig. 8 The variation of the β_{PI} versus δ for different values *of* ϑ ($k = 0.5$, $\xi = 0.3$, $\tau = 0.02$, $\Omega = 0.5$, $\bar{\omega} = 0$ and $\alpha = 0.1$)

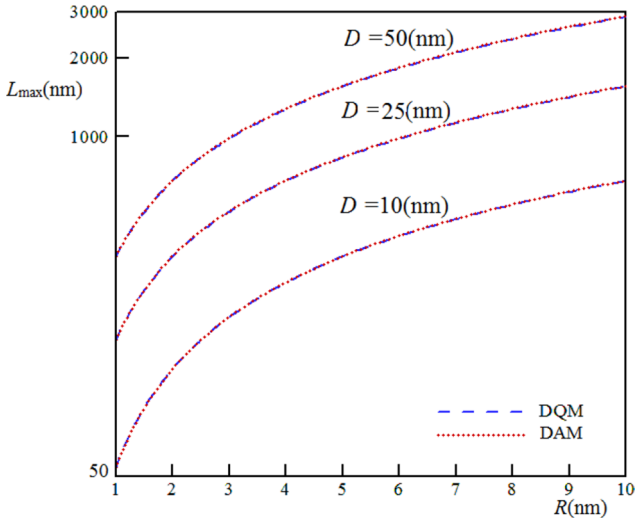

Fig. 9 Variation of L_{max} as a function of the radius of the nanowires and the initial gap in the absence of the centrifugal force ($\bar{\omega} = 0$) using $\delta = 0$, $a = 10$ nm and $b = 40$ nm

distances ($D = 50$ nm), increasing the angular speed leads to a significant decrease in the value of L_{max} of the nanowire.

4.3 Double-sided sensor

Figure 11a depicts the trend of the nanowire deflection for a typical double-sided sensor in the absence of the vdW and centrifugal forces ($\alpha = \bar{\omega} = 0$). The values of the parameters are selected as $k = 1.5$, $\xi = 2$, $\eta = 1.5$ and $\delta = 0$. Figure 11b, c shows the deflection of the nanowire ($\hat{w}$) in the presence of the vdW force ($\alpha = 0.4$, $\bar{\omega} = 0$) and for a

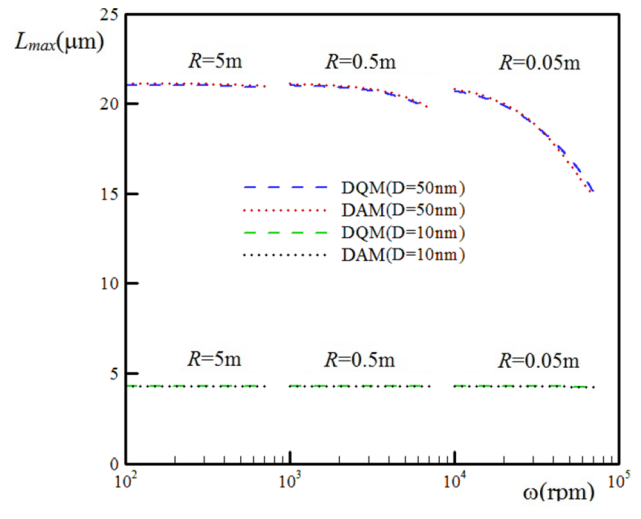

Fig. 10 Variation of L_{max} as a function of the angular speed of rotary surface and the initial gap for U-shaped nanosensors ($\rho = 2.1$ g/cm^3, $\delta = 0$, $r = 100$ nm, $a = 200$ nm and $b = 600$ nm)

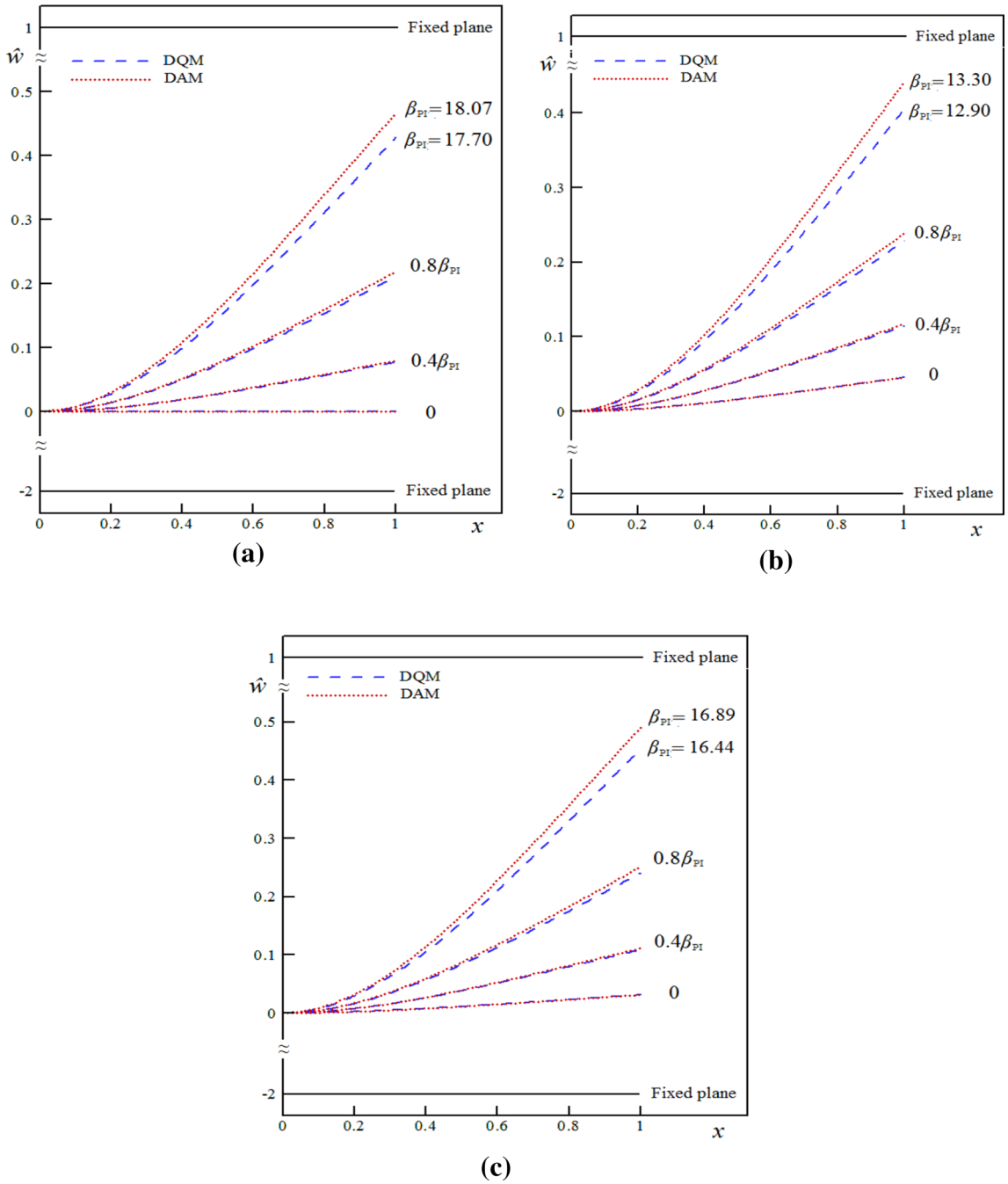

Fig. 11 Displacement variation of the nanowire for different values of β ($k = 1.5$, $\xi = 2$, $\eta = 1.5$, and $\delta = 0$); **a** neglecting the vdW and centrifugal forces, **b** considering the vdW force ($\bar{\omega} = 0, \alpha = 0.4$), **c** considering the centrifugal force ($\bar{\omega} = 0.25, \alpha = 0$)

positive value of the centrifugal force ($\bar{\omega} = 0.25$, $\alpha = 0$), respectively. Comparison between Fig. 11a, c shows that the positive value of the centrifugal force decreases the pull-in voltage while increasing the pull-in deflection of the sensor. On the other hand, the vdW force decreases the instability voltage of the system. Moreover, these figures show the initial deflection due to the vdW force, even when no electrostatic force has been applied.

Figure 12 depicts the variation of the tip deflection ($\hat{w}_{\text{tip}}$) versus the nondimensional voltage (β) for several values of the vdW force (α). As shown, for any applied voltage, where $\beta \leq \beta_{\text{PI}}$, solutions exist for $\hat{w}_{\text{tip}}$. On the other hand, when $\beta > \beta_{\text{PI}}$, no solution exists for $\hat{w}_{\text{tip}}$. This implies the occurrence of the instability, i.e. when the nanowire collapses onto and adheres to the fixed plane. At the instability threshold, the slope of the curves

approaches infinity ($d\hat{w}_{tip}/d\beta \rightarrow \infty$) which implies the feasibility of further deflection even without any increase in the electrostatic and, or, the vdW force(s). Also, Fig. 12 demonstrates that an increase of the vdW parameter (α) decreases the maximum tip displacement ($\hat{w}_{tip}$) of the nanowire.

The variation of the pull-in voltage of the double-sided sensor as a function of the centrifugal force is presented in Fig. 13 for various values of the size parameter. In this figure, both positive and negative values of the centrifugal force are considered. As shown, a negative centrifugal force increases the pull-in voltage (β_{PI}) while a positive centrifugal force decreases the instability voltage of the sensor. In other words, for positive values of the centrifugal force, an increase in the angular speed leads to a decrease of the pull-in voltage. On the other hand, increasing the angular velocity increases the stability threshold of the systems for negative values of the centrifugal force.

To examine the effect of geometry on the behavior of the double-sided sensor, variation of β_{PI} as a function of ξ is presented in Fig. 14 for various values of the vdW parameter α. The dimensionless parameter ξ represents the ratio between $\bar{D}$ and D. As shown, decreasing ξ increases the pull-in instability voltage. This reveals that decreasing the difference between D and $\bar{D}$ can stabilize the sensor. This is because the upper surface neutralizes the attractive effect of the lower surface.

Figure 15 displays the effect of the size parameter δ on the instability voltage of the nanowire. The zero value of δ corresponds to the classic continuum theory, i.e. the nanowire diameter is much larger than the intrinsic material length scale (l). According to Fig. 14, an increase in the size parameter (δ) increases the pull-in voltage of the sensor. Also, Fig. 14 shows the pull-in voltage decreases for an increase in ξ.

The value of L_{max} can be determined by computing α_{cr} (considering $\beta = 0$ and solving Eq. 24 for the double-sided structure), and then substituting α_{cr} into the definition of α (Eq. 23). The variation of L_{max} for a typical freestanding double-sided graphite sensor as a function of the nanowire radius and initial gap is shown in Fig. 16 by neglecting the centrifugal force. As shown in Fig. 16, increasing the gap distance and the diameter of nanowire leads to a significant increase in maximum permissible length of the wire L_{max}.

To examine the effect of the centrifugal force on the behavior of the freestanding double-sided sensor, variation of L_{max} versus the rotary surface radius and the angular speed for a typical centrifuge rotor ($R = 5$ cm), airplane propeller ($R = 0.5$ m), and helicopter blade ($R = 5$ m) is depicted in Fig. 17. As shown, increasing the angular speed and the rotation radius leads to a significant decrease in L_{max}. Moreover, the centrifugal force does not considerably alter L_{max} of sensors with a small separation ($D = 10$ nm). However, at larger distances ($D = 50$ nm), the effect of the centrifugal force on L_{max} is more pronounced.

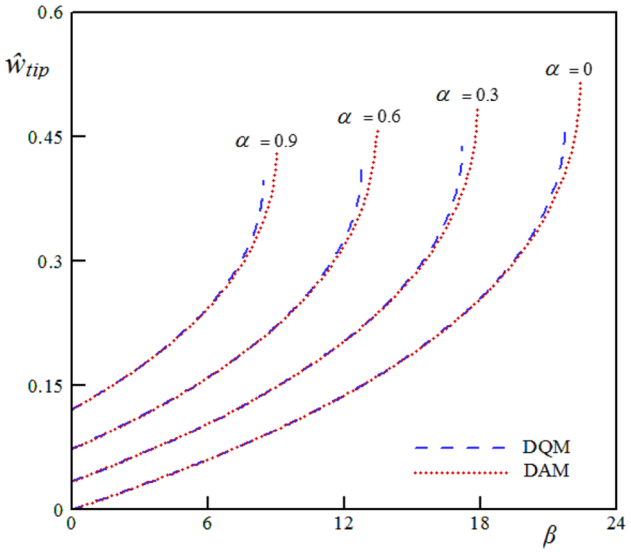

Fig. 12 The variation of $\hat{w}_{tip}$ versus β for various α values ($k = 2.0$, $\xi = 2.0$, $\eta = 1.0$, $\bar{\omega} = 0$ and $\delta = 0$)

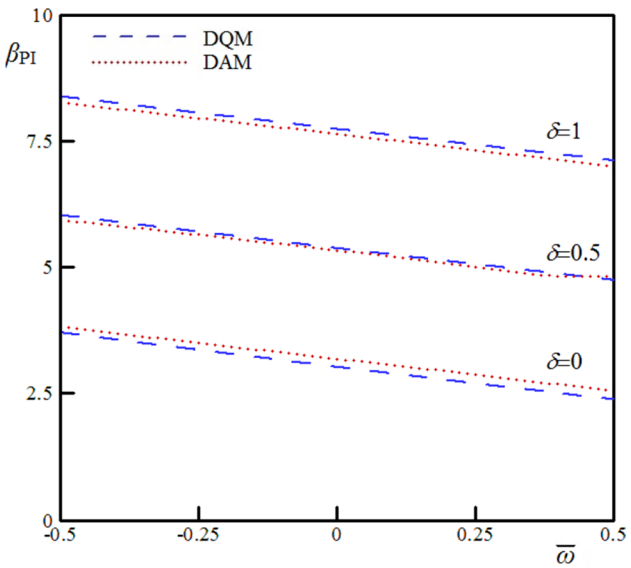

Fig. 13 The variation of the β_{PI} versus $\bar{\omega}$ for different values of ξ ($k = 0.5$, $\eta = 1.0$, $\alpha = 0.5$ and $\xi = 0$)

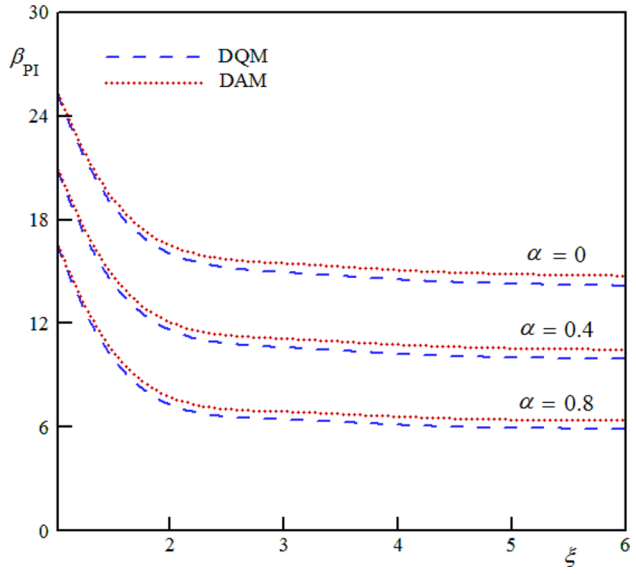

Fig. 14 The variation of the pull-in voltage versus ξ using $k = 1.5$, $\eta = 1.0$, $\bar{\omega} = 0$, $\delta = 0$, $\alpha = 0$, $\alpha = 0.4$ and $\alpha = 0.8$

5 Conclusions

Herein, the modified couple stress theory was applied for modeling the effect of the centrifugal force on the electromechanical instability of U-shaped and double-sided sensors incorporating the size-dependency and the vdW force. A general continuum model was developed and the governing equation of each nanostructure was solved using two different solution methods. A good agreement between the results of the numerical

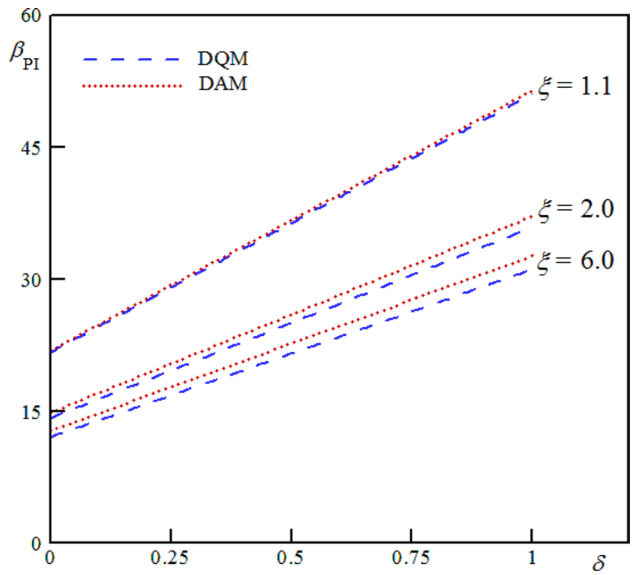

Fig. 15 The variation of the β_{PI} versus δ ($k = 2.0$, $\eta = 1.0$, $\bar{\omega} = 0$, $\alpha = 0.5$, $\xi = 1.1$, $\xi = 2.0$, $\xi = 6.0$)

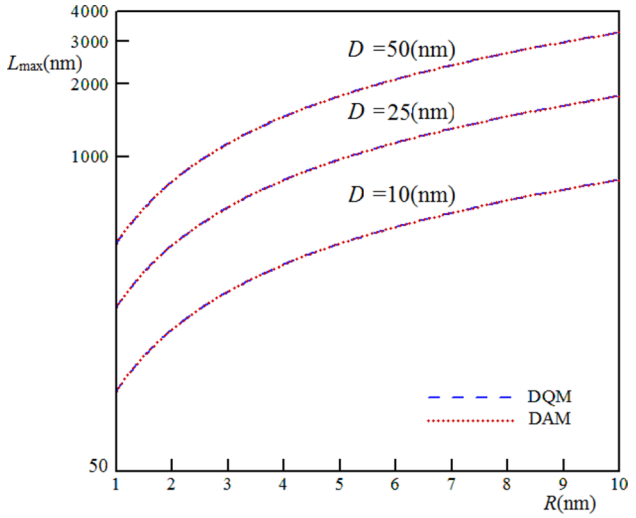

Fig. 16 Variation of L_{max} as a function of the wire diameter and initial gap ($\eta = 1.0$ and $\xi = 1.01$)

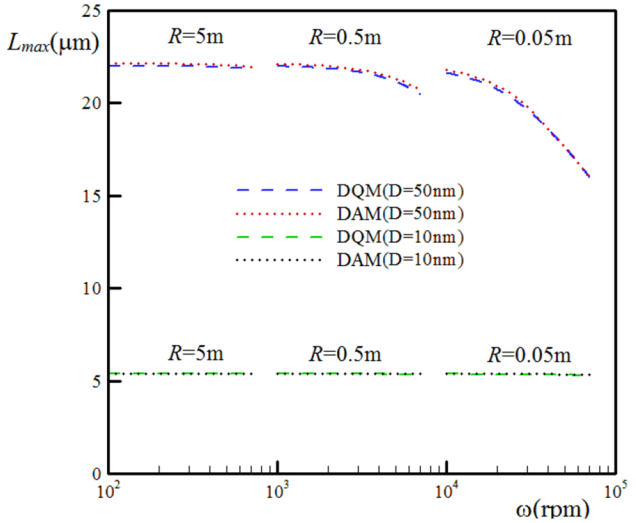

Fig. 17 Variation of L_{max} as a function of the angular speed of the rotary surface and the initial gap ($\rho = 2.1$ g/cm^3, $\delta = 0$, $r = 100$ nm, $\eta = 1.0$ and $\xi = 2$)

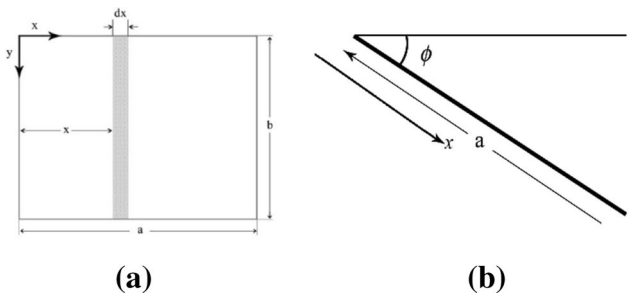

Fig. 18 Typical rigid plate and the integration element; **a** Top view, **b** side view

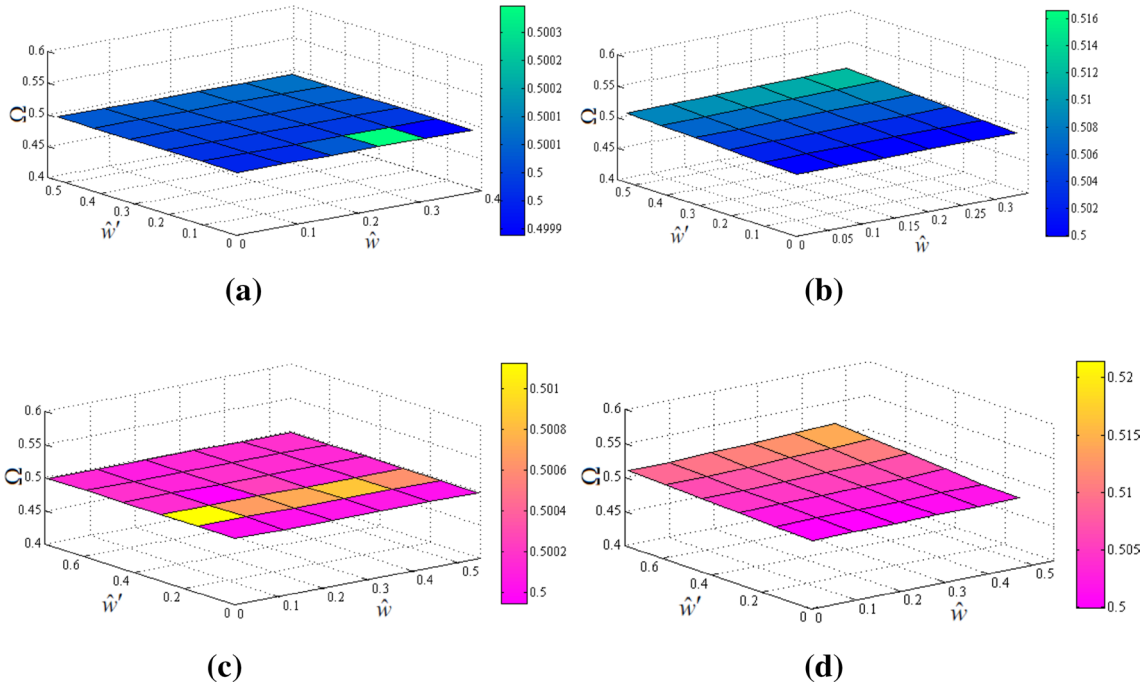

Fig. 19 The variation of Ω versus $\hat{w}$ and $\mathrm{d}\hat{w}/\mathrm{d}x$ using $\tau = 0.01$; **a** the vdW force ($\xi = 0.1$), **b** the vdW force ($\xi = 10$), **c** the electrostatic force ($\xi = 0.1$), **d** the electrostatic force ($\xi = 10$)

Table 1 The average value of Ω for different geometries

	vdW, $\xi = 0.1$	vdW, $\xi = 10.0$	Electrostatic, $\xi = 0.1$	Electrostatic, $\xi = 10.0$
Mean value of Ω	0.500	0.508	0.500	0.511
Max difference for F (%)	0.0	0.20	0	0
Max difference for M (%)	0.0	1.80	0.05	2.06

and analytic methods was observed. It was found that for positive values of the centrifugal force, the pull-in voltage decreases as the angular speed increases. On the other hand, for negative values of the centrifugal force, increases in the angular velocity increases the stability threshold of the systems. The variation of the detachment length of the freestanding sensors as a function of the centrifugal force was determined. It was found that the vdW attraction decreases, while the size effect increases, the pull-in voltage of the sensors. The pull-in voltage was significantly affected by the geometric characteristics of the nanostructures. The proposed approach and the obtained results are advantageous for the design and fabrication of U-shaped and double-sided angular speed measurement systems.

Appendix 1: Simplified boundary conditions of U-shaped structure

In Eq. (12), the force F and moment M are the summation of the force and moment due to the electrostatic, vdW and centrifugal forces which are calculated by integrating over the rigid plate area. Consider a typical rigid plate (Fig. 18) with the length a and width b, respectively.

The electrostatic, vdW and centrifugal forces acting on a differential element can be determined as

$$\mathrm{d}F_{\mathrm{elec}} = \frac{\varepsilon_0 V^2 b}{2(D - w(L) - x\sin(\varphi))^2}\mathrm{d}x, \tag{40a}$$

$$\mathrm{d}F_{\mathrm{vdW}} = \frac{Hb}{6\pi(D - w(L) - x\sin(\varphi))^3}\mathrm{d}x, \tag{40b}$$

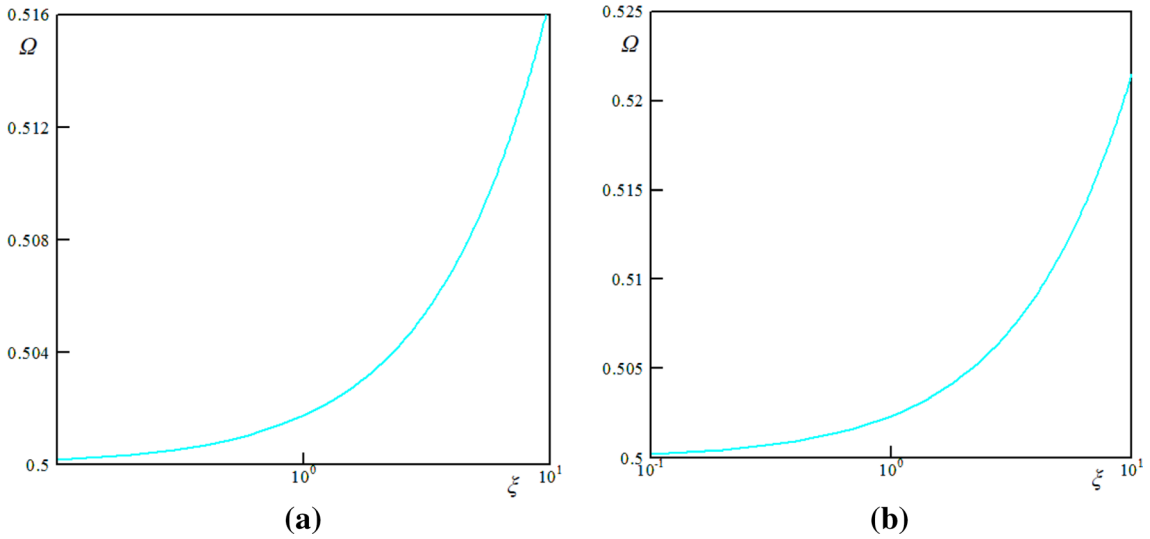

Fig. 20 The variation of the Ω versus ξ using the pull-in parameters; **a** the vdW force, **b** the electrostatic force

$$dF_{\text{Rot}} = \rho btR\omega^2 dx, \tag{40c}$$

where φ is the plate rotating angle that is determined from the following relation as

$$\tan(\varphi) = w'(L). \tag{41}$$

Therefore the electrostatic, vdW and centrifugal moments acting on each element are defined as

$$dM_{\text{elec}} = \frac{\varepsilon_0 V^2 b}{2(D - w(L) - x\sin(\varphi))^2} x\cos(\varphi)dx, \tag{42a}$$

$$dM_{\text{vdW}} = \frac{Hb}{6\pi(D - w(L) - x\sin(\varphi))^3} x\cos(\varphi)dx, \tag{42b}$$

$$dM_{\text{Rot}} = \rho btR\omega^2 x\cos(\varphi)dx. \tag{42c}$$

By using Eq. (40), the electrostatic, vdW and centrifugal forces can be determined as

$$F_{\text{elec}} = \int_0^a \frac{\varepsilon_0 V^2 b}{2(D - w(L) - x\sin(\varphi))^2} dx = \frac{\varepsilon_0 \varepsilon_r}{2} \frac{abV^2}{\left(D - w(L) - a\sqrt{\frac{w'^2(L)}{1+w'^2(L)}}\right)(D - w(L))}, \tag{43a}$$

$$F_{\text{vdW}} = \int_0^a \frac{Hb}{6\pi(D - w(L) - x\sin(\varphi))^3} dx = \frac{Hab\left[2D - 2w(L) - a\sqrt{\frac{w'^2(L)}{1+w'^2(L)}}\right]}{12\pi\left(D - w(L) - a\sqrt{\frac{w'^2(L)}{1+w'^2(L)}}\right)^2 (D - w(L))^2}, \tag{43b}$$

$$F_{\text{Rot}} = \int_0^a \rho btR\omega^2 dx = \rho abtR\omega^2, \tag{43c}$$

and for the moment as

$$M_{\text{elec}} = \int_0^a \frac{\varepsilon_0 V^2 b}{2(D - w(L) - x\sin(\varphi))^2} x\cos(\varphi)dx = \frac{\varepsilon_0 \varepsilon_r abV^2}{2} \frac{\sqrt{\frac{1}{1+w'^2(L)}}\left(\frac{D-w(L)}{a} - \sqrt{\frac{w'^2(L)}{1+w'^2(L)}}\right) Ln\left(\frac{D-w(L)-a\sqrt{\frac{w'^2(L)}{1+w'^2(L)}}}{D-w(L)}\right) + \frac{w'(L)}{1+w'^2(L)}}{\frac{w'^2(L)}{1+w'^2(L)}\left(D - w(L) - \sqrt{\frac{a^2 w'^2(L)}{1+w'^2(L)}}\right)}, \tag{44a}$$

$$M_{\mathrm{vdW}}=\int_0^a \frac{Hb}{6\pi\left(D-w(L)-x\sin(\varphi)\right)^3}x\cos(\varphi)\mathrm{d}x=\frac{Ha^2b\sqrt{\frac{1}{1+w'^2(L)}}}{12\pi\left(D-w(L)-a\sqrt{\frac{w'^2(L)}{1+w'^2(L)}}\right)^2\left(D-w(L)\right)}, \tag{44b}$$

$$M_{\mathrm{Rot}}=\int_0^a \rho btR\omega^2 x\cos(\varphi)\mathrm{d}x=\sqrt{\frac{1}{1+w'^2(L)}}\rho a^2btR\omega^2. \tag{44c}$$

The above relations describe the total forces and moments induced by the rigid plate. It should be noted that half of the forces and moment resultants should be considered as the contribution of each nanowire. By substituting Eqs. (44) and (45) into (12c) and using relations (23), the nondimensional exact boundary conditions are obtained as

$$\begin{aligned}(1+\delta)\frac{\mathrm{d}^2\hat{w}}{\mathrm{d}x^2}(1)=&\frac{\beta\tau\vartheta\left[\frac{(1-\hat{w}(1))\sqrt{1+\tau^2\hat{w}'^2(1)}}{\xi}-\tau\hat{w}'(1)\right]Ln\left[1-\frac{\xi\tau\hat{w}'(1)}{(1-\hat{w}(1))\sqrt{1+\tau^2\hat{w}'^2(1)}}\right]+\tau\hat{w}'(1)}{2k^{\frac{3}{2}}\tau^2\hat{w}'^2(1)(1-\hat{w}(1)-\frac{\xi\tau\hat{w}'(1)}{\sqrt{1+\tau^2\hat{w}'^2(1)}})}\\&+\frac{4\alpha\tau\xi\vartheta\frac{1}{\sqrt{1+\tau^2\hat{w}'^2(1)}}}{3k^{\frac{1}{2}}(1-\hat{w}(1))(1-\hat{w}(1)-\frac{\xi\tau\hat{w}'(1)}{\sqrt{1+\tau^2\hat{w}'^2(1)}})^2}+\frac{2\tau\xi\vartheta\,\bar{a}_z}{\sqrt{1+\tau^2\hat{w}'^2(1)}},\end{aligned} \tag{45a}$$

$$(1+\delta)\frac{\mathrm{d}^3\hat{w}}{\mathrm{d}x^3}(1)=-\frac{\beta\vartheta}{2k^{\frac{3}{2}}(1-\hat{w}(1)-\frac{\xi\tau\hat{w}'(1)}{\sqrt{1+\tau^2\hat{w}'^2(1)}})(1-\hat{w}(1))}-\frac{8\alpha\vartheta(2-2\hat{w}(1)-\frac{\xi\tau\hat{w}'(1)}{\sqrt{1+\tau^2\hat{w}'^2(1)}})}{3k^{\frac{1}{2}}(1-\hat{w}(1))^2(1-\hat{w}(1)-\frac{\xi\tau\hat{w}'(1)}{\sqrt{1+\tau^2\hat{w}'^2(1)}})^2}-4\vartheta\bar{a}_Z. \tag{45b}$$

Eq. (45a) is very complex, hence it cannot easily be used to find the solution of Eq. (22a). To obtain appropriate, simplified set of boundary conditions, the distributed forces acting on the rigid plate are replaced with an equivalent concentrated force acting at the force center ($\bar{x}$ from the beam tip). For any given values of $\hat{w}(1)$ and $\hat{w}'(1)$, the value of the dimensionless $\bar{x}$ (Ω) is obtained by equating the exact and approximate values of the force resultant (right-hand sides of Eqs. 22c and 45a). Figure 19 shows the variation of Ω for a wide range of values of the wire tip deflection and tip slope. This figure reveals that Ω is approximately constant for wide ranges of the deflection and slope values. The average values of Ω for different conditions of Fig. 19 are presented in Table 1. This table reveals that the overall error of the simplification is less than 2 % which is in the acceptable range. Moreover, variation of the parameter Ω for a wide range of geometries (ξ) is shown in Fig. 20. As shown, Ω is between 0.5 and 0.516 for the vdW force and between 0.5 and 0.525 for the electrostatic force. It can be concluded from this figure that for any geometry (ξ), a constant value of Ω can be approximately determined.

References

1. Ke CH, Espinosa HD (2006) Nanoelectromechanical systems (NEMS) and modeling. Handbook of theoretical and computational nanotechnology. American Scientific Publishers, Valencia
2. Rezazadeh G, Madinei H, Shabani R (2012) Study of parametric oscillation of an electrostatically actuated microbeam using variational iteration method. Appl Math Model 36(1):430–443
3. Sedighi HM, Shirazi KH (2013) Vibrations of micro-beams actuated by an electric field via parameter expansion method. Acta Astronaut 85:19–24
4. Rezazadeh G, Fathalilou M, Sadeghi M (2011) Pull-in voltage of electrostatically-actuated microbeams in terms of lumped model

pull-in voltage using novel design corrective coefficients. Sens Imaging Int J 12(3–4):117–131
5. Zand MM, Ahmadian MT (2010) Dynamic pull-in instability of electrostatically actuated beams incorporating Casimir and van der Waals forces. Proc Inst Mech Eng Part C J Mech Eng Sci 224(9):2037–2047
6. Koochi A, Kazemi A, Abadyan M (2011) Simulating deflection and determining stable length of freestanding carbon nanotube probe/sensor in the vicinity of graphene layers using a nanoscale continuum model. NANO 6(05):419–429
7. Koochi A, Kazemi AS, Noghrehabadi A, Yekrangi A, Abadyan M (2011) New approach to model the buckling and stable length of multi walled carbon nanotube probes near graphite sheets. Mater Des 32(5):2949–2955
8. Latorre L, Nouet P, Bertrand Y, Hazard P, Pressecq F (1999) Characterization and modeling of a CMOS-compatible MEMS technology. Sens Actuators A 74(1):143–147
9. Yan D, Khajepour A, Mansour R (2004) Design and modeling of a MEMS bidirectional vertical thermal actuator. J Micromech Microeng 14(7):841
10. Qian Y, Lou L, Tsai MJ, Lee C (2012) A dual-silicon-nanowires based U-shape nanoelectromechanical switch with low pull-in voltage. Appl Phys Lett 100(11):113102
11. Koukharenko E, Beeby SP, Tudor MJ, White NM, O'Donnell T, Saha C, Kulkarni S, Roy S (2006) Microelectromechanical systems vibration powered electromagnetic generator for wireless sensor applications. Microsyst Technol 12(10–11):1071–1077
12. Lee KB (2007) Closed-form solutions of the parallel plate problem. Sens Actuators A 133(2):518–525
13. Kopka P, Hoffmann M, Voges E (2000) Coupled U-shaped cantilever actuators for 1 × 4 and 2 × 2 optical fibre switches. J Micromech Microeng 10(2):260
14. Keplinger F, Beigelbeck R, Kohl F, Kvasnica S, Jachimowicz A, Jakoby B (2005) Frequency and transient analysis of micromachined U-shaped cantilever devices for magnetic field measurement. In: IEEE The 13th international conference on solid-state sensors, actuators and microsystems, 2005. Digest of technical papers. TRANSDUCERS'05, vol 1, pp 630–635
15. Sedighi HM, Shirazi KH (2015) Dynamic pull-in instability of double-sided actuated nano-torsional switches. Acta Mech Solida Sin 28(1):901–101
16. Fu Y, Zhang J, Wan L (2011) Application of the energy balance method to a nonlinear oscillator arising in the microelectromechanical system (MEMS). Curr Appl Phys 11(3):482–485
17. Ke C (2009) Resonant pull-in of a double-sided driven nanotube-based electromechanical resonator. J Appl Phys 105(2):024301
18. Bao M (2005) Analysis and design principles of MEMS devices. Elsevier, Amsterdam
19. Khan Y, Akbarzade M (2012) Dynamic analysis of nonlinear oscillator equation arising in double-sided driven clamped microbeam-based electromechanical resonator. Z Naturforschung A J Phys Sci 67(8):435
20. Sedighi HM, Shirazi KH (2015) Effect of the amplitude of vibrations on the pull-in instability of double-sided actuated microswitch resonators. J App Mech Tech Phys 56(2):304–312
21. Dashtaki PM, Tadi Beni Y (2014) Effects of Casimir force and thermal stresses on the buckling of electrostatic nanobridges based on couple stress theory. Arabian J Sci Eng 39(7):5753–5763
22. Bodson M, Chiasson J, Novotnak RT (1995) Nonlinear speed observer for high-performance induction motor control. IEEE Trans Ind Electron 42(4):337–343
23. Renaudin L, Bonnardot F, Musy O, Doray JB, Rémond D (2010) Natural roller bearing fault detection by angular measurement of true instantaneous angular speed. Mech Syst Signal Process 24(7):1998–2011
24. Lebold MS, Maynard K, Reichard K, Trethewey M, Bieryla D, Lissenden C, Dobbins D (2004) Using torsional vibration analysis as a synergistic method for crack detection in rotating equipment. In: Proceedings of the 2004 IEEE aerospace conference, vol 6, pp 3517–3527
25. Jywe WY, Chen CJ (2005) The development of a high-speed spindle measurement system using a laser diode and a quadrants sensor. Int J Mach Tools Manuf 45(10):1162–1170
26. Huang CT, Li PN, Pai CY, Leu TS, Jen CP (2009) Design and simulation of a microfluidic blood-plasma separation chip using microchannel structures. Sep Sci Technol 45(1):42–49
27. Hou C, Wu Y, Zeng X, Zhao S, Zhou Q, Yang G (2010) Novel high sensitivity accelerometer based on a microfiber loop resonator. Opt Eng 49(1):014402
28. Azimloo H, Rezazadeh G, Shabani R, Sheikhlou M (2014) Bifurcation analysis of an electro-statically actuated micro-beam in the presence of centrifugal forces. Int J Non-Linear Mech 67:7–15
29. Shah-Mohammadi-Azar A, Azimloo H, Rezazadeh G, Shabani R, Tousi B (2013) On the modeling of a capacitive angular speed measurement sensor. Measurement 46(10):3976–3981
30. Soroush R, Koochi A, Kazemi AS, Noghrehabadi A, Haddadpour H, Abadyan M (2010) Investigating the effect of Casimir and van der Waals attractions on the electrostatic pull-in instability of nano-actuators. Phys Scr 82(4):045801
31. Abdi J, Koochi A, Kazemi AS, Abadyan M (2011) Modeling the effects of size dependence and dispersion forces on the pull-in instability of electrostatic cantilever NEMS using modified couple stress theory. Smart Mater Struct 20(5):055011
32. Wang GW, Zhang Y, Zhao YP, Yang GT (2004) Pull-in instability study of carbon nanotube tweezers under the influence of van der Waals forces. J Micromech Microeng 14(8):1119
33. Van Spengen WM, Puers R, De Wolf I (2002) A physical model to predict stiction in MEMS. J Micromech Microeng 12(5):702
34. Farrokhabadi A, Rach R, Abadyan M (2013) Modeling the static response and pull-in instability of CNT nanotweezers under the Coulomb and van der Waals attractions. Phys E 53:137–145
35. Farrokhabadi A, Abadian N, Rach R, Abadyan M (2014) Theoretical modeling of the Casimir force-induced instability in freestanding nanowires with circular cross-section. Phys E 63:67–80
36. Farrokhabadi A, Mokhtari J, Rach R, Abadyan M (2014) Modeling the influence of the Casimir force on the pull-in instability of nanowire-fabricated nanotweezers. Int J Mod Phys B 29(02):1450245
37. Lam DCC, Yang F, Chong ACM, Wang J, Tong P (2003) Experiments and theory in strain gradient elasticity. J Mech Phys Solids 51(8):1477–1508
38. McFarland AW, Colton JS (2005) Role of material microstructure in plate stiffness with relevance to microcantilever sensors. J Micromech Microeng 15(5):1060
39. Yang FACM, Chong ACM, Lam DCC, Tong P (2002) Couple stress based strain gradient theory for elasticity. Int J Solids Struct 39(10):2731–2743
40. Park SK, Gao XL (2006) Bernoulli-Euler beam model based on a modified couple stress theory. J Micromech Microeng 16(11):2355
41. Tsiatas GC (2009) A new Kirchhoff plate model based on a modified couple stress theory. Int J Solids Struct 46(13):2757–2764
42. Beni YT, Karimipöur I, Abadyan M (2014) Modeling the effect of intermolecular force on the size-dependent pull-in behavior of beam-type NEMS using modified couple stress theory. J Mech Sci Technol 28(9):3749–3757
43. Beni YT, Koochi A, Abadyan M (2014) using modified couple stress theory for modeling the size-dependent pull-in instability of torsional nano-mirror under Casimir force. Int J Optomech 8(1):47–71

44. Koochi A, Kazemi AS, Tadi Beni Y, Yekrangi A, Abadyan M (2010) Theoretical study of the effect of Casimir attraction on the pull-in behavior of beam-type NEMS using modified Adomian method. Phys E 43(2):625–632
45. Farrokhabadi A, Koochi A, Kazemi A, Abadyan M (2014) Effects of size-dependent elasticity on stability of nanotweezers. Appl Math Mech Engl Ed 35(12):1573–1590
46. Jackson JD (1998) Classical electrodynamics. Wiely, New York
47. Hayt WH (1981) Engineering electromagnetics. McGraw-Hill, New York
48. Israelachvili JN (2011) Intermolecular and surface forces: revised, 3rd edn. Academic press, Cambridge
49. Duan JS (2011) Convenient analytic recurrence algorithms for the Adomian polynomials. Appl Math Comput 217(13):6337–6348
50. Adomian G (1986) Nonlinear stochastic operator equations. Academic Press, Orlando
51. Duan JS (2010) An efficient algorithm for the multivariable Adomian polynomials. Appl Math Comput 217(6):2456–2467
52. Shu C (2000) Differential quadrature and its application in engineering. Springer, Berlin
53. Koochi A, Farrokhabadi A, Abadyan M (2015) Modeling the size dependent instability of NEMS sensor/actuator made of nano-wire with circular cross-section. Microsyst Technol 21(2):355–364
54. Ke CH, Pugno N, Peng B, Espinosa HD (2005) Experiments and modeling of carbon nanotube-based NEMS devices. J Mech Phys Solids 53(6):1314–1333
55. Lin WH, Zhao YP (2005) Nonlinear behavior for nanoscale electrostatic actuators with Casimir force. Chaos Solitons Fractals 23(5):1777–1785